Novel fabrication tools for dynamic compression targets with engineered voids using photolithography methods

Silvia Pandolfi[1+], Thomas Carver[2*], Daniel Hodge[3], Andrew F.T. Leong[4], Kelin Kurzer-Ogul[5], Philip Hart[1], Eric Galtier[1], Dimitri Khaghani[1], Eric Cunningham[1], Bob Nagler[1], Hae J. Lee[1], Cindy Bolme[4], Kyle Ramos[4], Kenan Li[1], Yanwei Liu[1], Anne Sakdinawat[1], Stefano Marchesini[1], Pawel M. Kozlowski[4], Chandra B. Curry[1,6], Franz-Joseph Decker[1], SharonVetter[1], Jessica Shang[5,7], Hussein Aluie[5,7], Matthew Dayton[8], David S. Montgomery[4], Richard L. Sandberg[3], Arianna E. Gleason[1].*

[1]SLAC National Accelerator Laboratory, 2575 Sand Hill Rd, Menlo Park, CA, USA, 94025
[2] Stanford Nano Shared Facilities, Stanford University, Palo Alto, CA, USA, 94305
[3]Brigham Young University, Department of Physics and Astronomy, Provo, UT, USA, 84602
[4] Los Alamos National Laboratory, Los Alamos, NM, USA, 87545
[5] Department of Mechanical Engineering, University of Rochester, Rochester, New York 14623, USA
[6] Department of Electrical and Computer Engineering, University of Alberta, Edmonton, Alberta T6G 1H9, Canada
[7]Laboratory for Laser Energetics, University of Rochester, Rochester, New York 14623, USA
[8]Advanced hCMOS Systems, 6300 Riverside Plaza Ln Suite 100, Albuquerque, NM, USA, 87107

**authors contributed equally*
[+] The author to whom correspondence may be addressed: silviap@stanford.edu

Abstract:
Mesoscale imperfections, such as pores and voids, can strongly modify the properties and the mechanical response of materials under extreme conditions. Tracking the material response and microstructure evolution during void collapse is crucial for understanding its performance. In particular, imperfections in ablator materials, such as voids, can limit the efficiency of the fusion reaction and ultimately hinder ignition. To characterize how voids influence the response of materials during dynamic loading and seed hydrodynamic instabilities, we have developed a tailored fabrication procedure for designer targets with voids at specific locations. Our procedure uses SU-8 as a proxy for ablator materials and hollow silica microspheres as proxy for voids and pores. By using photolithography to design the targets' geometry, we demonstrate precise and highly reproducible placement of a single void within the sample, which is key for a detailed understanding of its behavior under shock compression. This fabrication technique will benefit high-repetition rate experiments at x-ray and laser facilities. Insight from shock compression experiments will provide benchmarks for the next generation of microphysics modelling.

I.INTRODUCTION

Mesoscale imperfections and inhomogeneities in structure and composition play a crucial role in the physical and chemical behavior of all materials. The mechanical properties and response of materials, especially at extreme conditions, *e.g.*, at pressures above a Mbar, are largely dictated by microstructure and defect content. Material defects can be planar at domain interfaces or grain boundaries, linear like dislocations, or at a single point or location in a structure, such as chemical impurities or vacancies. An accumulation of defects or vacancies in any material can lead to void or pore space formation. The need to understand how voids and the void collapse process dictate materials performance under extreme conditions intersects many materials science applications and a range of disciplines, such as geophysics[1], planetary- and fusion energy sciences[2,3].

Characterization of the response of void defects and void collapse during dynamic compression is critical for predicting the microphysics dictating the material's response – as the collapse process can seed hydrodynamic instabilities[4–9]. One area of study where the material properties and the seeding of instabilities is particularly problematic is Inertial Confinement Fusion (ICF) physics[10]. Here, uniform spherical implosion of a fuel inside a capsule is necessary to generate thermonuclear ignition[11,12]; potentially, ignition could open an exciting area of research for future global clean energy solutions, termed Inertial Fusion Energy (IFE)[13–16]. However, the presence of defects, particularly voids, in the ablator layer, *i.e.*, outermost material of the capsule, has been recognized as one of the major contributions to performance degradation due to instability seeding and growth[17]. Micron-sized voids and pores in the ablator layer have been suggested to possibly cause jetting as the collapse process generates ejecta with roughly double the particle velocity of the bulk material, launching Rayleigh-Taylor hydrodynamic instabilities[18–20], which limits compression of the fuel and fusion performance. A precise understanding of the response of mesoscale defects, such as voids, in the ablator material, is thus key for advancing ICF and IFE.

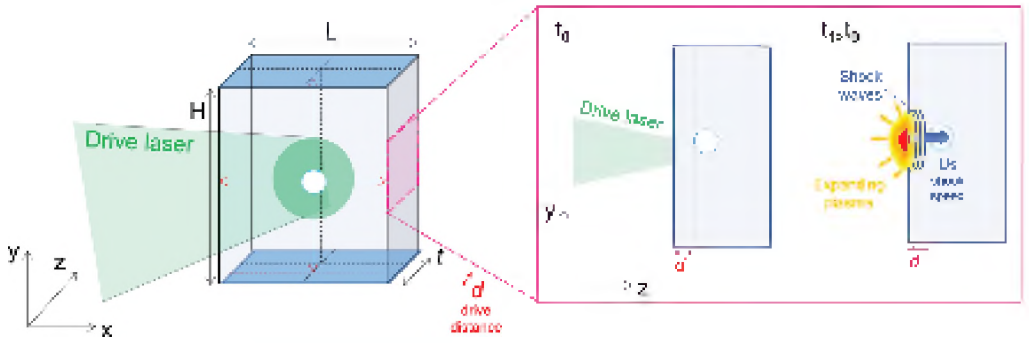

Figure 1. Left: schematic view of ideal sample for void collapse; the compression is driven by a high-power laser focused on the sample's drive surface (*x*-*y* plane). The inset on the right shows the working principle of laser-driven shock-compression: the formation of an expanding plasma at the drive surface generates shock waves that compress the sample along the laser propagation direction (*z*).

New experimental benchmark data are required to refine current microphysics models of void collapse under shock compression, which include a combination of material strength, radiation transport, instability tracking, equation of state and transport properties[21]. To specifically tackle understanding of how voids dictate a material's response to dynamic compression, a well-characterized void feature is needed. To do this, we created a fabrication procedure to enable design and characterization of a simplified system, *i.e.*, an isolated void and its interaction with the propagating shock wave and the surrounding material. Dynamic compression is achieved by focusing a high-power laser onto the sample to generate ablation-driven shock compression (Figure 1, right panel). As shown in Figure 1, a specific placement of the void within the sample is required by the experimental geometry. To ensure homogeneous spatial compression, the void needs to be centered with respect to the drive surface, *i.e.*, the *xy*-plane in Figure 1. Furthermore, the distance between the void and the drive surface (*d* along the *z*-axis in Figure 1) should be tunable.

Future x-ray free electron laser (XFEL) experiments, with the expected upgrades of optical driver lasers to 1Hz frequency, will be conducted at high-repetition rates and will require large-scale target production[22] (*i.e.,* one sample and one compression every second, compared to the current shot cycle of 5-7 minutes). To satisfy these requirements, there is an ongoing effort in the community to develop new strategies for mass scale production of samples. Recently, Smith et al. have demonstrated a novel fabrication procedure for slurry targets that uses particles embedded in epoxy to produce "ribbons" of materials[22]. Here, we present photolithography-based fabrication of targets for dynamic compression containing isolated voids. This method allows for large-scale production of individual designer targets with tuned microstructures and properties, a key requirement for the study of mesoscale imperfections under dynamic compression. Precise and reproducible placement of an isolated void within the sample is viable with this methodology; the study of such simplified systems will provide precise and detailed insight into the behavior of micron-sized voids under dynamic compression. This fabrication method can also be extended to other fields of high-energy density science, *e.g.*, viscosity measurements that use isolated heterogeneities embedded in the bulk[23–25]. Large-scale, designer target fabrication procedures will also be key in the development of the IFE industry, where 10 Hz rep-rated laser technology could drive the foundational design of future fusion power plants[26].

II.METHOD

II.A Materials

Polystyrene $(C_8H_8)_n$ and other plastic materials, *e.g.* glow deposition polymer[27–30], are commonly used as ablator materials in ICF experiments. Here, to investigate their properties and the interaction of defects with a propagating shock wave, we have used the photoresist SU-8[31] as a proxy. SU-8, made by Kayaku Advanced Materials, is a mixture of photosensitive epoxy resin, epoxy novolac polymer, and various solvents. The mixture is a viscous liquid that can be easily deposited and spun into layers. That is to say, SU-8 can be deposited onto a substrate, and, by fast rotation, the SU-8 solution is distributed via centrifugal force resulting in a homogenous coverage, while the excess material is ejected; several layers of SU-8 can be spun on top of each other before exposure and hardening[32]. The solvents and their proportions can be manipulated to achieve different viscosities, which can produce layers with thicknesses ranging from 0.5μm to >200 μm. The vendor provides calibrated spinning protocols indicating the approximate thickness that can be obtained depending on spinning speed, duration and on the viscosity of the starting SU-8 material. The SU-8 epoxy cross-links and hardens when exposed to ultraviolet light (optimal wavelength 365 nm), and the unexposed parts can be dissolved[33]. By using appropriate photolithography masks, this allows the production of geometries with high precision.

The experimental requirements for these targets are multifaceted – not only they need to be similar in properties and shock response to traditional polymer ICF ablators, but they also need to have uniform thickness for dynamic X-ray imaging measurements and be uniform laterally for steady shock propagation. SU-8 has similar density (1.2 g/cm^3)[34], mechanical (Young's modulus 4.1 GPa)[35] and optical (refractive index 1.6)[36] properties as polystyrene[37]. The practical advantages when using SU-8 as a proxy for other polymers is that being a photoresist it can be spun over a substrate to obtain a homogeneous layer. Moreover, photolithography enables production of devices with specific geometries and a resolution on the order of few micrometers. The final result is an optically transparent device whose thickness can be specified by spinning various formulations of SU-8 of the appropriate viscosity (commercially available) and tuning the spinning speed and duration. In particular, for our study the quality of the lateral walls is crucial, and SU-8 enables control and fabrication of nearly vertical sidewalls, even in devices with very

high aspect ratios [38–40]: this will ensure the planarity of the driven shock as well as the ability to

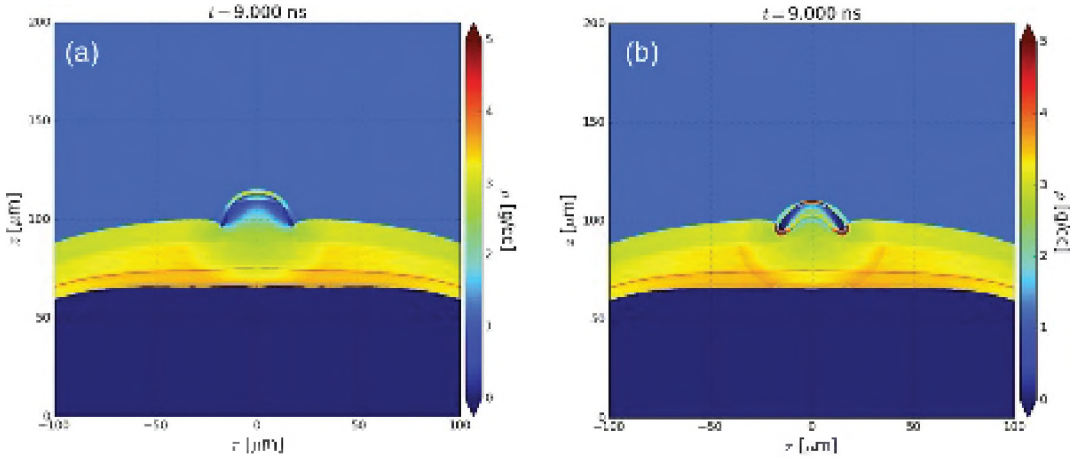

Figure 2. Hydrodynamic simulations of shock-compressed SU-8 embedding: (a) a 40 μm spherical void, (b) a 40 μm hollow SiO_2 shell with 2 μm-thick walls.

use a suite of characterizations, *e.g.*, velocimetry for pressure measurements[41] or X-ray based imaging techniques[42–46].

In our fabrication procedure, we used hollow silica glass shells as a proxy for the actual voids. Such hollow glass shells are commercially available (Cospheric LLC) as microspheres made of a proprietary soda-lime borosilicate formulation, with nominal wall thicknesses up to a few μm. Hollow microspheres with metallic coatings are also available, which can be used to tune their mechanical as well as conductive properties. Thanks to the small thickness of the microsphere silica shell (estimates ~1.5 μm), the behavior of our devices under shock-compression is consistent with that of a device containing an actual void of the same size, as shown in Figure 2. Hydrodynamic simulations show similar flows and polymer density for shock-compression of a 40-μm void and a 40-μm silica shell with 2 μm-thick walls, demonstrating that the hollow microsphere behavior can provide physically-significant insight into the physics of voids collapse. There are numerous advantages in using silica microspheres over other void-fabrication techniques like laser milling: (i) versatility, as the microspheres are available in a wide range of sizes 5-125 μm; (ii) cost reduction, as the microspheres can be purchased in large quantities and are relatively inexpensive; (iii) time-saving, as for each SU-8 spinning numerous void-bearing devices can be produced, as opposed to the time required to prepare the bare devices and individually laser-mill the desired void for each device. Furthermore, the ability to produce many samples with a single spinning procedure also ensures high homogeneity within each batch. The effectiveness and scalability of this fabrication approach procedure make it suitable for the next

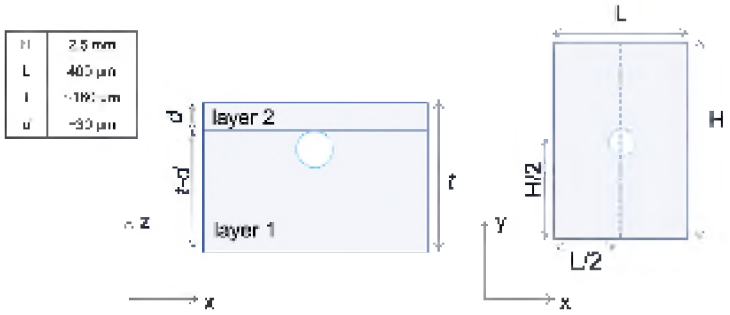

Figure 3. Schematic view of ideal sample geometry for X-ray imaging experiment under shock compression.

generation of ICF and high-energy density XFEL-based experiments, as it can meet the increased need for targets once high repetition rate driver lasers are available.

II.B Experimental procedure

The ideal target design for ICF void-bearing ablators is shown in Figure 3. As previously mentioned, the void should be centered in the laser drive surface (x*y*-plane) and placed at a specific distance *d* from the drive surface (i.e., along the *z*-axis). Specifically, for our experiments we used ~40 µm hollow silica microspheres (HSG 38-45ect) and the desired *d* value was ~30 µm. However, the size of the microsphere as well as the device's dimensions can easily be tuned using this fabrication procedure. We developed our fabrication procedure at the Stanford Nano Shared Facilities (SNSF) at Stanford University, CA (USA). SU-8 was spun onto a substrate using a Headway PWM32-PS-CB15 spinner; several layers can be superposed before exposure, allowing to build up stratified devices of the desired thickness *t*. For our experiments, we have used a 3" silicon wafer as substrate, and spun over different metal layers (*i.e.*, 50 nm of copper adhesion layer and titanium coating) to increase the adhesion and thickness uniformity of the photoresist during spinning. The microspheres were heated at 150°C for about 15-20 minutes to dry out adsorbed moisture on the surfaces and separate beads that were clumped together, allowing them to fall individually.
From preliminary tests with the 40 µm microspheres, we have noticed full wetting of the beads after dispersion onto an unexposed SU-8 layer, so we designed the target fabrication as follows. For a device of desired thickness *t* and bead-drive distance *d* (see Figure 1-2): (i) spin a layer of SU-8 of thickness *t-d*; (ii) deposit the bead, by either sprinkling them or by singularly place them onto the substrate; (iii) spin an additional layer of SU-8 of thickness *d*. In this way, the microspheres are fully wetted by the layer 1 and sink to the level, so *d* can be directly tuned by changing the spinning parameters of layer 2. The parameters from our optimized fabrication procedure are reported in Table 1. We have used the SU-8 2050 solution as starting material for both layers. Even though, nominally, the final SU-8 density should not depend on the viscosity of the starting material, using only one solution throughout the whole fabrication ensured to obtain a more homogenous device, avoiding eventual microstructural or density inhomogeneities.

Layer	Thickness	Value [µm]	Spin speed [RPM]	Ramp [RPM/s]	Time [s]	Bake temp. [°C]	Bake time [min]
Layer 1	*t-d*	130	500	100	10	65; 95	7; 40
			1500	300	30		
Deposit hollow microspheres							
Layer 2	*d*	30	500	100	10	95	5
			3300	300	30		

Table 1. explanation of parameters

Within the SNSF, a Durham Magneto Optics ML3 MicroWriter direct write (maskless) exposure machine operating at 385 nm was available. Despite 385nm not being the optimal wavelength to cross-link SU-8, the photoresist could still be successfully processed by increasing the exposure dose to achieve full cross-link (Figure 4). Further experimentation with dose and defocus helped to enhance the sidewall geometry to make optically smooth, near vertical sidewalls. With respect to our procedure, the exposure dose and processing time can be reduced by using the most suited 365 nm UV wavelength. We used the microscope of the direct write machine to examine

the substrate and the SU-8 and to locate the beads. The center of the beads is easily detected, as the spheres exhibit a bright reflection from their exact center; we used this bright reflection to determine their coordinates in X and Y with ~1-micron accuracy. For exposure and cross-link, a rectangular mask of the desired dimensions (in our case 400 µm x 2.5 mm) was designed and centered in X and Y, which ensured precise placement of the bead in the *xy*-plane of the device (Figure 3, right panel). The machine can be set up to expose the rectangular patterns sequentially on the microsphere's coordinates, allowing to produce several devices for each exposure; this approach can be readily expanded to different target and/or bead placement geometries simply modifying the exposure mask design. By varying the exposure dose, different results in terms of SU-8 cross-link and edge sharpness can be obtained, as shown in Figure 4. For example, 2000 mJ/cm^2 is not sufficient to fully expose the SU-8: the device appears opaque at the optical microscope, which suggests that the bottom layer is partially unexposed and thus does not exhibit the optical quality and transparence of fully cross-linked SU-8. No noticeable changes are observed varying the exposure dose between 2200 and 2600 mJ/cm^2, and the devices appear transparent with sharp edges; for exposure doses of 2800 mJ/cm^2 and higher, the corner starts to look less sharp and darker at the optical microscope. The darker edges and corners indicate that the sidewalls of the devices are slightly tiled, with a larger cross-linked area toward the bottom of the device; this results from overexposure, as at the bottom layer is crossed-linked not only from direct irradiation, but also from non-perpendicular light reflected by the metallic coating on the substrate. While overexposure slightly affects the vertical sidewalls, it also ensures that the whole devices, down to the substrate, is fully cross-linked. For our optimized fabrication procedure, we used a 10X microscope, and lens setting with nominal exposure resolution of 1µm; we estimate our actual resolution to be of the order of 2-3 µm, as we slightly overexposed our devices to ensure complete cross-link of the epoxy and good mechanical properties under shock-compression (3000 mJ/cm^2, see Figure 4). Slight over-exposure was preferred for this protocol to compensate eventual shadowing from the microsphere, as shown in Figure 7 and discussed in the following section. It is worth noting that, because the positions of the microspheres are individuated and recorded manually one at a time the uncertainty on the bead placement within the device depends solely on the microscope and on the direct write machine resolutions, and is thus of the order of 2-3 µm, without being affected by the batch size.

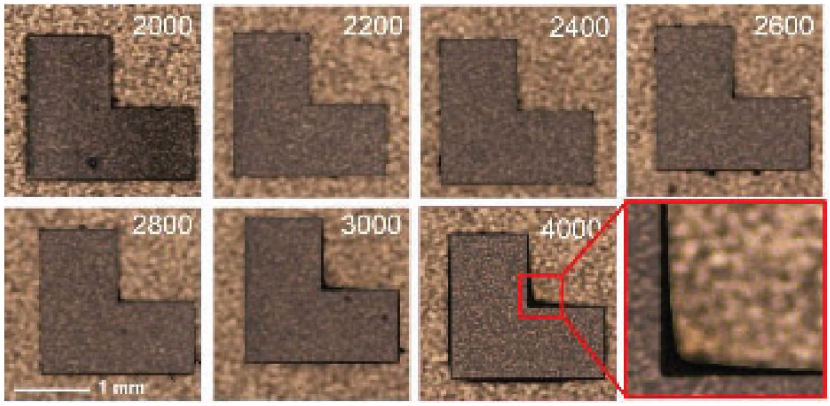

Figure 4. Example of exposure tests, in which the exposure dose was systematically changed; the numbers on each figure indicate the exposure dose for each device (expressed in mJ/cm^2).

After exposure, the spun SU-8 was baked at 65° for 5 minutes and then at 95° for 13 minutes. Subsequently, the whole wafer was submerged in SU-8 Developer (mfg. by Kayaku Materials) for 15 minutes and gently turned to dissolve all the non-exposed photoresist. After this step, only the exposed cross-linked region, *i.e.*, the devices, remain on the substrate while the rest of the SU-8

is dissolved and rinsed away. After development and full cross-link, the SU-8 adhesion to the substrate decreases, and the devices can be mechanically detached from the substrate using a fine and anti-scratch tweezer for leverage. We have tested other extraction methods, such as dissolving a sacrificial layer of Al or Cu, but we have discovered that the metal etchants unexpectedly dissolve the SU-8 and/or compromise the optical quality of the devices' walls. However, the possibility of mechanically extract the devices simplifies the procedure, as it doesn't require rinsing, filtering, and recovering of the parts from the etchants.
Furthermore, we noted the use of a metallic layer on top of the Si substrate facilitates mechanical extraction of the devices, which can be easily peeled off the wafer without damages. The final step for completing curing and hardening of the extracted targets was a 10-minute bake at 150°C.

III.RESULTS

Following the procedure detailed in Section II, up to 50-60 void-bearing SU-8 devices can be fabricated from a single SU-8 processing, ensuring high homogeneity within each batch. After completing the fabrication, we used X-ray computed tomography (CT) to determine whether the procedure had affected the voids; the results are shown in Figure 5. X-ray CT is a non-destructive scanning X-ray imaging technique that, by collecting angle-resolved X-ray images of the sample, can provide reconstructed 2D slices at specific depths within the sample[47]. Figure 5(a) shows the reconstructed slice at the center of the device; the microsphere size (~40μm diameter) and the void depth *d* (~30 μm) are consistent with the expected values. Importantly, X-ray absorption was measured along the yellow line in Figure 5(a). The results are reported in Figure 5(b) and show that the region inside the void display the same X-ray absorption as the air surrounding the device, which implies that no chemical or solvent penetrates the glass walls, and the microspheres remain empty throughout the whole fabrication procedure. Thus, the hollow silica microspheres embedded in cross-linked SU-8 following our experimental protocol are a suitable proxy for actual voids within the sample.

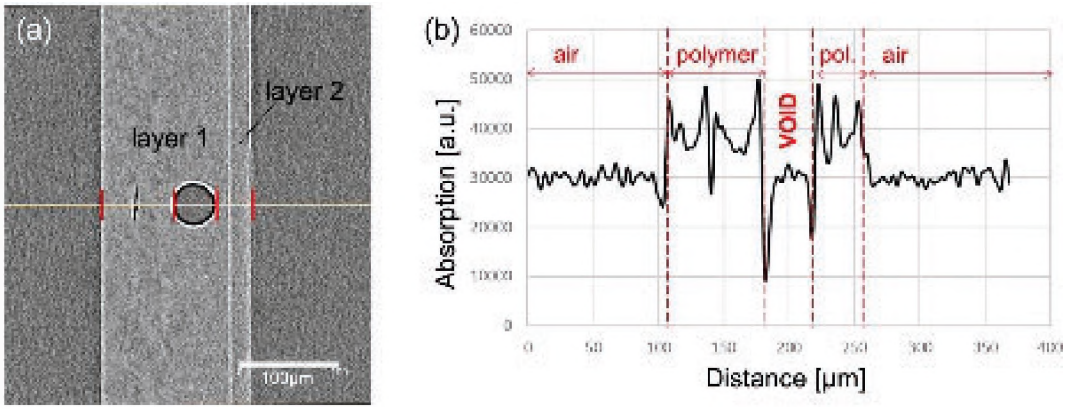

Figure 5. X-ray CT measurements of a representative eSU-8 void-bearing target (Carl Zeiss X-ray Microscopy Inc. Xradia Versa 520). (a) 2D reconstructed slice at the void center. (b) X-ray absorption as measured along the yellow line in (a); the different parts and materials are indicated.

We performed further imaging characterization to confirm the microsphere placement within the device, as well as checking the optical quality of the devices' lateral walls; the results are reported in Figure 6. The optical image in Figure 6 (c,d) shows the "top view", which corresponds to the *xy*-plane in Figures 1-2, *i.e.*, the surface on which the driver laser is focused for laser-driven shock-compression. As previously mentioned, shock-compression experiments require the voids to be centered in this surface to ensure planar and homogeneous compression. Precise placement of

the microsphere was successful using photolithography to cross-link the SU-8 in a region centered around an isolated microsphere (Sect. II-B). We have also analyzed the placement of the void along the direction of the shock propagation, *i.e.*, the *z*-axis in Figures 1-2. The optical image reported in Figure 6(a) shows that our results are consistent with the desired value of ~30 μm, thus the fabrication procedure allows us to accurately define this distance by optimizing the spinning conditions of the second SU-8 layer (Sect. II-B). However, optical measurements through a transparent medium could be affected by aberrations, especially when looking at the "side view", as the images are collecting through a 400 μm-thick layer of SU-8. For this reason, we have also used X-ray imaging techniques (X-ray CT in Figure 5 and XFEL-based X-ray imaging in Figure 6(b)) to confirm the value and the reproducibility of the desired void-drive distance *d*. Our fabrication procedure is thus suited for the design of devices embedding voids at specific locations, as shown in Figure 6, and the results were highly reproducible over hundreds of devices. It is also worth noting that our ability to obtain clear images of the beads through 100μm up to 400 μm of SU-8 demonstrates the high optical quality of the devices' lateral walls.

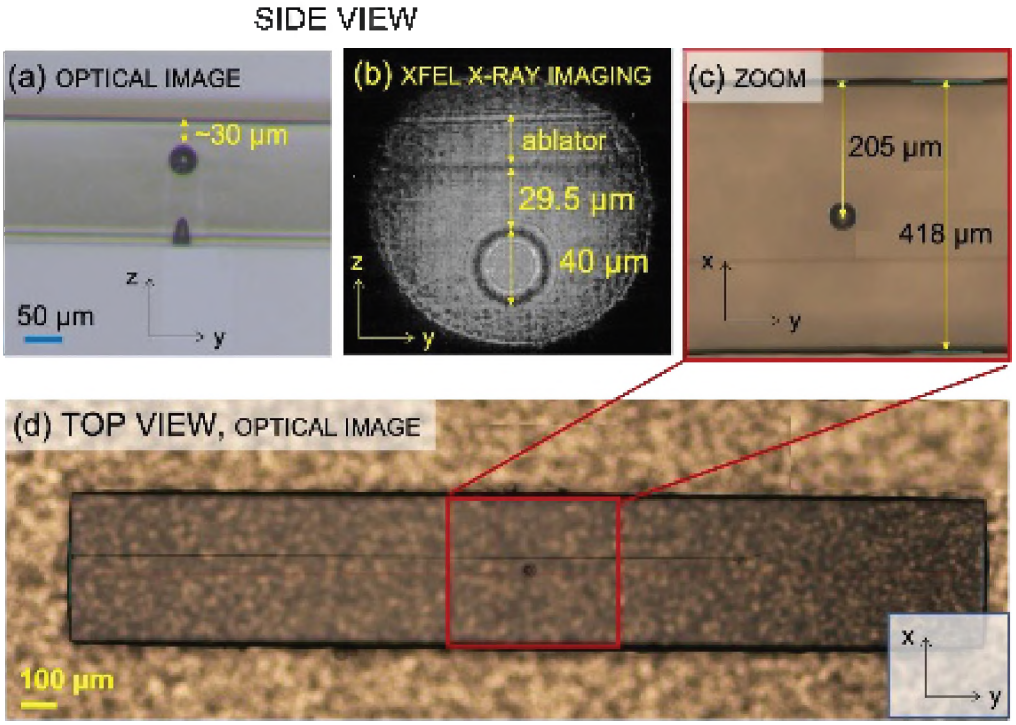

Figure 6. Representative images of void-bearing SU-8 targets; both optical (a,c,d) and x-ray (b) images confirm the production of targets with the desired geometry.

As detailed in Sect. II-B, we have spun the thick layer incorporating the voids first, and then a second layer to ensure that the microspheres are at the desired depth *d* within the sample. Besides the advantage of an easily tunable procedure to optimize *d*, this choice was also dictated by the necessity to ensure full exposure through the total thickness of the device. Indeed, the microspheres dispersed in the SU-8 can cause shadowing during the photolithography process and affect full cross-link of the region beneath them; results from our preliminary tests are reported in Figure 7. As visible by the "side view" of these devices, having the microsphere on top of a thick layer (Figure 7(a)) can mitigate the shadowing effects experienced by a microsphere placed

closer to the wafer substrate (Figure 7(b)). It is probable, indeed, that having more space between the silica shell and the metallic substrate allows for more photons to be reflected from the metallic surface of the substrate. Thus, even if not by direct irradiation, the region beneath the microsphere is still exposed, and it cross-links. On the contrary, when the microsphere is too close to the bottom of the device, the shadowing effects dominate, and the region beneath it is not exposed such that the sphere sinks to the bottom, as shown in Figure 7(b). This further emphasizes the importance of the slight overexposure of the device that we adopted. Indeed, not only it ensures cross-link of bare SU-8, but also full exposure beneath the microsphere, in the region shadowed from direct irradiation.

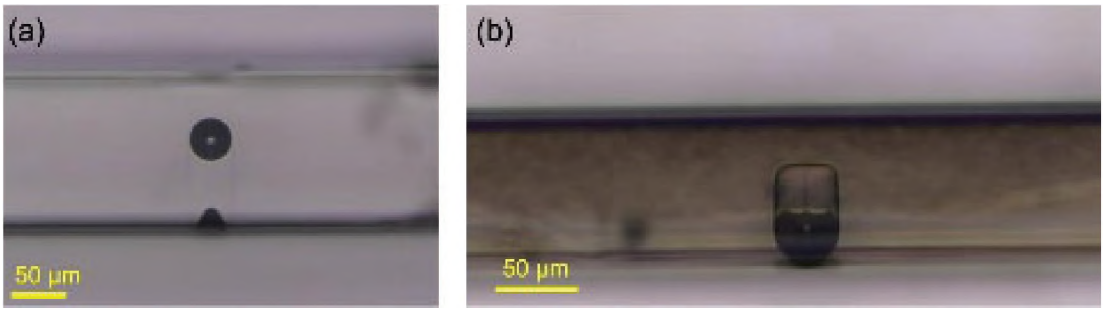

Figure 7. Optical microscopy images showing the effects of shadowing from the microsphere over the SU-8 cross-link. (a) shadowing is mitigated by spinning the thicker layer first; (b) when the microsphere is closer to the substrate, the region beneath it is not cross-linked and the sphere sinks to the bottom.

IV.SUMMARY

We have developed and tested a fabrication procedure that allows for large-scale production of void-bearing targets for dynamic compression experiments. We used SU-8 photoresist and hollow silica microspheres as proxies for void-bearing ICF ablator materials. Our fabrication procedure exploits spinning of SU-8 layers at the designated thicknesses and the use of specifically designed photolithography masks to ensure placement of the void at a desired location within the target. Imaging and absorption data confirm the viability of this approach and the reproducibility of the results over hundreds of targets. Furthermore, production of up to 50-60 targets can be achieved within a single fabrication procedure, ensuring high uniformity over several tens of devices. Scalability and high reproducibility make this technique suited for future studies at high repetition rate, and the fabrication details can be also optimized for different experimental scopes, *e.g.*, using metal-coated or filled spheres for viscosity measurements.

ACKNOWLEDMENTS

This work is supported by the U.S. Department of Energy (DOE) Office of Science, Office of Fusion Energy Sciences under the Early Career Award, 2019 for A. Gleason. Part of this work was performed at the Stanford Nano Shared Facilities (SNSF), supported by the National Science Foundation under award ECCS-2026822. Research presented in this article was supported by the Laboratory Directed Research and Development program of Los Alamos National Laboratory under project numbers 20200744PRD1 and 20210717ER. We are grateful for the work from B. M. Patterson, MST-7, LANL and X-ray CT data using the Carl Zeiss X-ray Microscopy Inc. Xradia Versa 520.
JKS was supported by US NSF grant PHY-2020249, US DOE DE-SC0019329, and US NNSA grant DE-NA0003914. KKO was also supported by US NNSA grant DE-NA0003914. HA was also supported by US DOE grants DE-SC0014318, DE-SC0019329, and US NNSA grant DE-

NA0003914. CBC was also supported by US DOE, Office of Science, Office of Fusion Energy Sciences under FWP100182. Part of the work presented here was carried out at the MEC instrument of the Linac Coherent Light Source (LCLS). Use of the LCLS, SLAC National Accelerator Laboratory, is supported by the U.S. Department of Energy, Office of Science, Office of Basic Energy Sciences under Contract No. DE-AC02-76SF00515. the MEC instrument has additional support from the U.S. DOE, Office of Science, Office of Fusion Energy Sciences under contract No. SF00515.

References

[1] D.B. Larson and G.D. Anderson, J Geophys Res Solid Earth 84, 4592 (1979).
[2] R.A. Sacks and D.H. Darling, Nucl Fusion 27, 447 (1987).
[3] R.E. Olson, M.J. Schmitt, B.M. Haines, G.E. Kemp, C.B. Yeamans, B.E. Blue, D.W. Schmidt, A. Haid, M. Farrell, P.A. Bradley, H.F. Robey, and R.J. Leeper, Phys Plasmas 28, 122704 (2021).
[4] Y.T. Nguyen, D. Perera, P. Zhao, T. Sewell, and H.S. Udaykumar, Propellants Explos Pyrotech (2022).
[5] Z. Ding and S.M. Gracewski, J Fluid Mech 309, 183 (1996).
[6] N.A. Hawker and Y. Ventikos, J Fluid Mech 701, 59 (2012).
[7] J.H.J. NIEDERHAUS, J.A. GREENOUGH, J.G. OAKLEY, D. RANJAN, M.H. ANDERSON, and R. BONAZZA, J Fluid Mech 594, 85 (2007).
[8] D. Ranjan, M. Anderson, J. Oakley, and R. Bonazza, Phys Rev Lett 94, 184507 (2005).
[9] D. Ranjan, J. Oakley, and R. Bonazza, Fluid Mech 43, 117 (2011).
[10] S.J. Ali, P.M. Celliers, S. Haan, T.R. Boehly, N. Whiting, S.H. Baxamusa, H. Reynolds, M.A. Johnson, J.D. Hughes, B. Watson, H. Huang, J. Biener, K. Engelhorn, V.A. Smalyuk, and O.L. Landen, Phys Plasmas 25, 092708 (2018).
[11] R. Betti and O.A. Hurricane, Nat Phys 12, 435 (2016).
[12] R.S. Craxton, K.S. Anderson, T.R. Boehly, V.N. Goncharov, D.R. Harding, J.P. Knauer, R.L. McCrory, P.W. McKenty, D.D. Meyerhofer, J.F. Myatt, A.J. Schmitt, J.D. Sethian, R.W. Short, S. Skupsky, W. Theobald, W.L. Kruer, K. Tanaka, R. Betti, T.J.B. Collins, J.A. Delettrez, S.X. Hu, J.A. Marozas, A.V. Maximov, D.T. Michel, P.B. Radha, S.P. Regan, T.C. Sangster, W. Seka, A.A. Solodov, J.M. Soures, C. Stoeckl, and J.D. Zuegel, Phys Plasmas 22, 110501 (2015).
[13] V.T. Tikhonchuk, Philosophical Transactions Royal Soc 378, 20200013 (2020).
[14] D. SC, *Fusion Energy Sciences Advisory Committee Long Range Planning Report, "Powering the Future: Fusion & Plasmas"* (2021).
[15] A.L. Kritcher, A.B. Zylstra, D.A. Callahan, O.A. Hurricane, C. Weber, J. Ralph, D.T. Casey, A. Pak, K. Baker, B. Bachmann, S. Bhandarkar, J. Biener, R. Bionta, T. Braun, M. Bruhn, C. Choate, D. Clark, J.M.D. Nicola, L. Divol, T. Doeppner, V. Geppert-Kleinrath, S. Haan, J. Heebner, V. Hernandez, D. Hinkel, M. Hohenberger, H. Huang, C. Kong, S.L. Pape, D. Mariscal, E. Marley, L. Masse, K.D. Meaney, M. Millot, A. Moore, K. Newman, A. Nikroo, P. Patel, L. Pelz, N. Rice, H. Robey, J.S. Ross, M. Rubery, J. Salmonson, D. Schlossberg, S. Sepke, K. Sequoia, M. Stadermann, D. Strozzi, R. Tommasini, P. Volegov, C. Wild, S. Yang, C. Young, M.J. Edwards, O. Landen, R. Town, and M. Herrmann, Phys Plasmas 28, 072706 (2021).
[16] A.B. Zylstra, O.A. Hurricane, D.A. Callahan, A.L. Kritcher, J.E. Ralph, H.F. Robey, J.S. Ross, C.V. Young, K.L. Baker, D.T. Casey, T. Döppner, L. Divol, M. Hohenberger, S.L. Pape, A. Pak, P.K. Patel, R. Tommasini, S.J. Ali, P.A. Amendt, L.J. Atherton, B. Bachmann, D. Bailey, L.R. Benedetti, L.B. Hopkins, R. Betti, S.D. Bhandarkar, J. Biener, R.M. Bionta, N.W. Birge, E.J. Bond, D.K. Bradley, T. Braun, T.M. Briggs, M.W. Bruhn, P.M. Celliers, B. Chang, T. Chapman, H. Chen, C. Choate, A.R. Christopherson, D.S. Clark, J.W. Crippen, E.L. Dewald, T.R. Dittrich, M.J. Edwards, W.A. Farmer, J.E. Field, D. Fittinghoff, J. Frenje, J. Gaffney, M.G. Johnson, S.H. Glenzer, G.P. Grim, S. Haan, K.D. Hahn, G.N. Hall, B.A. Hammel, J. Harte, E. Hartouni, J.E. Heebner, V.J. Hernandez, H. Herrmann, M.C. Herrmann, D.E. Hinkel, D.D. Ho, J.P. Holder, W.W. Hsing, H. Huang, K.D. Humbird, N. Izumi, L.C. Jarrott, J. Jeet, O. Jones, G.D. Kerbel, S.M. Kerr, S.F. Khan, J. Kilkenny, Y. Kim, H.G. Kleinrath, V.G. Kleinrath, C. Kong, J.M. Koning, J.J. Kroll, M.K.G. Kruse, B. Kustowski, O.L. Landen, S. Langer, D. Larson, N.C. Lemos, J.D. Lindl, T. Ma, M.J. MacDonald, B.J. MacGowan, A.J. Mackinnon, S.A. MacLaren, A.G. MacPhee, M.M. Marinak, D.A. Mariscal, E.V. Marley, L. Masse, K. Meaney, N.B. Meezan, P.A. Michel, M. Millot, J.L. Milovich, J.D. Moody, A.S. Moore, J.W. Morton, T. Murphy, K. Newman, J.-M.G.D. Nicola, A. Nikroo, R. Nora, M.V.

Patel, L.J. Pelz, J.L. Peterson, Y. Ping, B.B. Pollock, M. Ratledge, N.G. Rice, H. Rinderknecht, M. Rosen, M.S. Rubery, J.D. Salmonson, J. Sater, S. Schiaffino, D.J. Schlossberg, M.B. Schneider, C.R. Schroeder, H.A. Scott, S.M. Sepke, K. Sequoia, M.W. Sherlock, S. Shin, V.A. Smalyuk, B.K. Spears, P.T. Springer, M. Stadermann, S. Stoupin, D.J. Strozzi, L.J. Suter, C.A. Thomas, R.P.J. Town, E.R. Tubman, P.L. Volegov, C.R. Weber, K. Widmann, C. Wild, C.H. Wilde, B.M.V. Wonterghem, D.T. Woods, B.N. Woodworth, M. Yamaguchi, S.T. Yang, and G.B. Zimmerman, Nature 601, 542 (2022).
[17] V.A. Smalyuk, C.R. Weber, O.L. Landen, S. Ali, B. Bachmann, P.M. Celliers, E. Dewald, A. Fernandez, B.A. Hammel, G. Hall, A.G. MacPhee, L. Pickworth, H.F. Robey, N. Alfonso, K.L. Baker, L.F.B. Hopkins, L. Carlson, D.T. Casey, D.S. Clark, J. Crippen, L. Divol, T. Döppner, J. Edwards, M. Farrell, S. Felker, J.E. Field, S.W. Haan, A.V. Hamza, M. Havre, M.C. Herrmann, W.W. Hsing, S. Khan, J. Kline, J.J. Kroll, S. LePape, E. Loomis, B.J. MacGowan, D. Martinez, L. Masse, M. Mauldin, J.L. Milovich, A.S. Moore, A. Nikroo, A. Pak, P.K. Patel, J.L. Peterson, K. Raman, B.A. Remington, N. Rice, M. Schoff, M. Stadermann, and S.A. Yi, High Energ Dens Phys 36, 100820 (2020).
[18] R.E. Kidder, Nucl Fusion 16, 3 (1976).
[19] L. Soulard, N. Pineau, J. Clérouin, and L. Colombet, J Appl Phys 117, 115901 (2015).
[20] J.D. Kilkenny, S.G. Glendinning, S.W. Haan, B.A. Hammel, J.D. Lindl, D. Munro, B.A. Remington, S.V. Weber, J.P. Knauer, and C.P. Verdon, Phys Plasmas 1, 1379 (1994).
[21] S.X. Hu, V.N. Goncharov, P.B. Radha, S.P. Regan, and E.M. Campbell, Nucl Fusion 59, 032011 (2018).
[22] R.F. Smith, V. Rastogi, A.E. Lazicki, M.G. Gorman, R. Briggs, A.L. Coleman, C. Davis, S. Singh, D. McGonegle, S.M. Clarke, T. Volz, T. Hutchinson, C. McGuire, D.E. Fratanduono, D.C. Swift, E. Folsom, C.A. Bolme, A.E. Gleason, F. Coppari, H.J. Lee, B. Nagler, E. Cunningham, P. Heimann, R.G. Kraus, R.E. Rudd, T.S. Duffy, J.H. Eggert, and J.K. Wicks, J Appl Phys 131, 245901 (2022).
[23] Altshuler, L. and Doronin, and G. and Kim, Appl Mech Tech Phys 110 (1987).
[24] G.Kh. Kim, J Appl Mech Tech Ph+ 25, 692 (1984).
[25] D.B. Bober, J. Lind, and M. Kumar, Phys Rev Mater 3, 073603 (2019).
[26] FESAC, *Powering the Future - Fusion & Plasmas* (2020).
[27] S.W. Haan, H. Huang, M.A. Johnson, M. Stadermann, S. Baxamusa, S. Bhandarkar, D.S. Clark, V. Smalyuk, and H.F. Robey, Phys Plasmas 22, 032708 (2015).
[28] H. S and et al., *Haan, S. et al. Comparison of the Three NIF Ablators. Internal Report LLNL-TR-741418 (2017).* (2017).
[29] Cook and et al., *Preliminary Evaluation of Techniques to Fabricate Beryllium, Polyimide, and Ge-Doped CH/CD Ablator Materials. LLNL Internal UCRL-TR-208476* (2004).
[30] S.J. Ali, P.M. Celliers, S.W. Haan, T.R. Boehly, N. Whiting, S.H. Baxamusa, H. Reynolds, M.A. Johnson, J.D. Hughes, B. Watson, K. Engelhorn, V.A. Smalyuk, and O.L. Landen, Phys Rev E 98, 033204 (2018).
[31] J.M. Shaw, J.D. Gelorme, N.C. LaBianca, W.E. Conley, and S.J. Holmes, Ibm J Res Dev 41, 81 (1997).
[32] J. Orava, T. Kohoutek, and T. Wagner, Part Prep Prop Chalcogenide Glasses 265 (2014).
[33] Z.-F. Zhou and Q.-A. Huang, Micromachines-Basel 9, 341 (2018).
[34] I. Roch, P. Bidaud, D. Collard, and L. Buchaillot, J Micromech Microeng 13, 330 (2003).
[35] T. Xu, J.H. Yoo, S. Babu, S. Roy, J.-B. Lee, and H. Lu, J Micromech Microeng 26, 105001 (2016).
[36] T.C. Sum, A.A. Bettiol, J.A. van Kan, F. Watt, E.Y.B. Pun, and K.K. Tung, Appl Phys Lett 83, 1707 (2003).
[37] S.A. Saq'an, A.S. Ayesh, A.M. Zihlif, E. Martuscelli, and G. Ragosta, Polym Test 23, 739 (2004).
[38] K.-Y. Hung and T.-H. Liang, Microsyst Technol 14, 1217 (2008).
[39] A. del Campo and C. Greiner, J Micromech Microeng 17, R81 (2007).
[40] J. Liu, B. Cai, J. Zhu, G. Ding, X. Zhao, C. Yang, and D. Chen, Microsyst Technol 10, 265 (2004).
[41] D.H. Dolan, (2006).
[42] S.B. Brown, A.E. Gleason, E. Galtier, A. Higginbotham, B. Arnold, A. Fry, E. Granados, A. Hashim, C.G. Schroer, A. Schropp, F. Seiboth, F. Tavella, Z. Xing, W. Mao, H.J. Lee, and B. Nagler, Sci Adv 5, eaau8044 (2019).
[43] R.L. Sandberg, C. Bolme, K. Ramos, Q. McCulloch, R. Martinez, V. Hamilton, T. Pierce, M. Greenfield, K. Brown, S. McGrane, J.L. Barber, B. Abbey, A. Schropp, F. Seiboth, P. Heiman, B. Nagler, E. Galtier, and E. Granados, Int Conf Ultrafast Phenom UTh4A.36 (2016).

[44] A. Schropp, R. Hoppe, V. Meier, J. Patommel, F. Seiboth, Y. Ping, D.G. Hicks, M.A. Beckwith, G.W. Collins, A. Higginbotham, J.S. Wark, H.J. Lee, B. Nagler, E.C. Galtier, B. Arnold, U. Zastrau, J.B. Hastings, and C.G. Schroer, Sci Rep-Uk 5, 11089 (2015).
[45] R.L. Sandberg, C. Bolme, K. Ramos, Q. McCulloch, R. Martinez, V. Hamilton, T. Pierce, M. Greenfield, S. McGrane, J.L. Barber, B. Abbey, A. Schropp, F. Seiboth, P. Heiman, B. Nagler, E. Galtier, and E. Granados, Microsc Microanal 21, 1851 (2015).
[46] B. Nagler, A. Schropp, E.C. Galtier, B. Arnold, S.B. Brown, A. Fry, A. Gleason, E. Granados, A. Hashim, J.B. Hastings, D. Samberg, F. Seiboth, F. Tavella, Z. Xing, H.J. Lee, and C.G. Schroer, Rev Sci Instrum 87, 103701 (2016).
[47] P.J. Withers, C. Bouman, S. Carmignato, V. Cnudde, D. Grimaldi, C.K. Hagen, E. Maire, M. Manley, A.D. Plessis, and S.R. Stock, Nat Rev Methods Primers 1, 18 (2021).

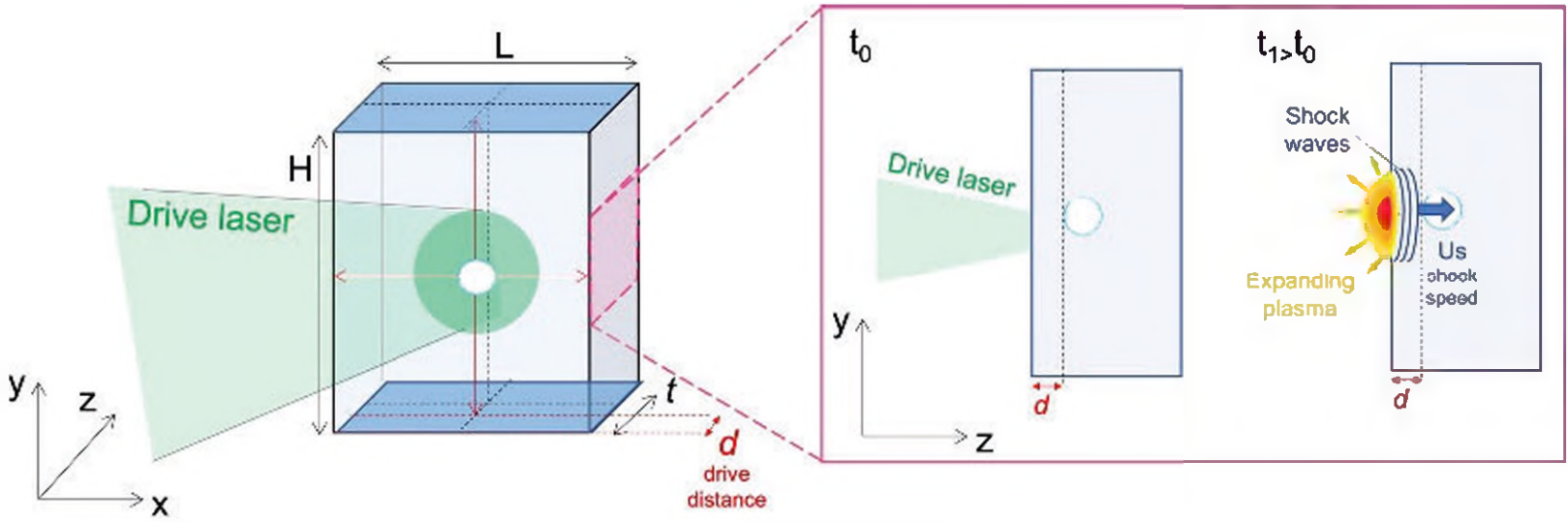
L
H
Drive laser
t
d
drive
distance
y
z
x
t_0
Drive laser
d
y
z
$t_1 > t_0$
Shock
waves
Expanding
plasma
Us
shock
speed
d

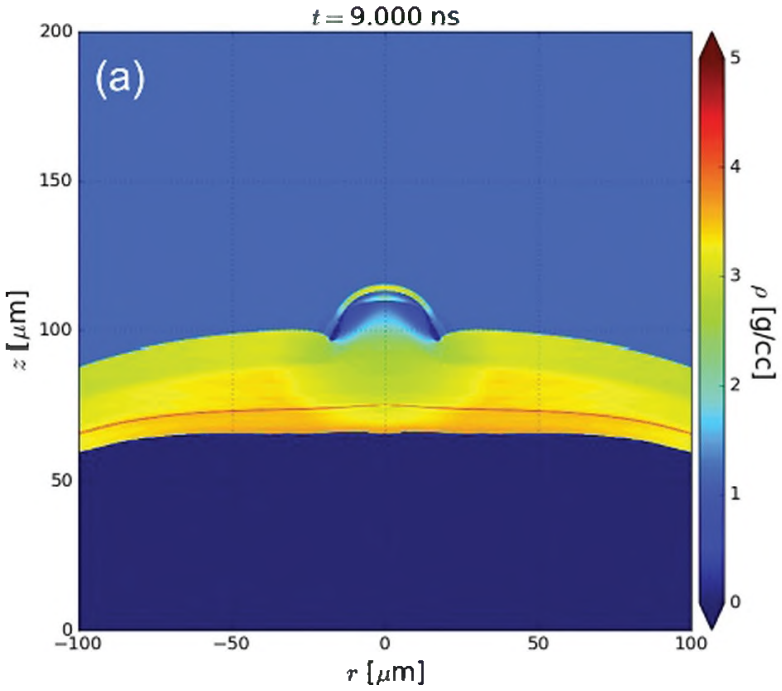
$t = 9.000$ ns
(a)
200
150
100
50
0
z [μm]
−100
−50
0
50
100
r [μm]
5
4
3
2
1
0
ρ [g/cc]

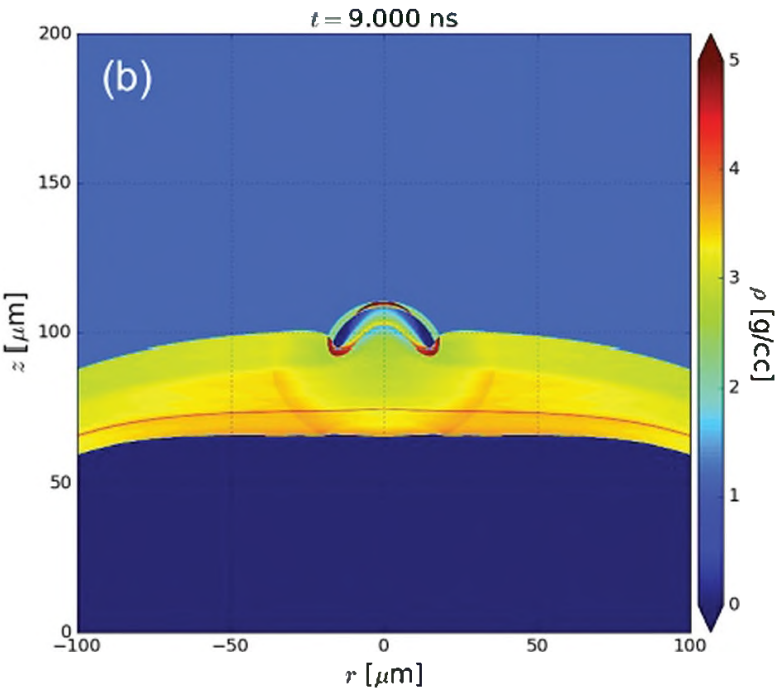
$t = 9.000$ ns
(b)
200
150
100
50
0
z [μm]
−100
−50
0
50
100
r [μm]
5
4
3
2
1
0
ρ [g/cc]

H	2.5 mm
L	400 µm
t	~160 µm
d	~30 µm

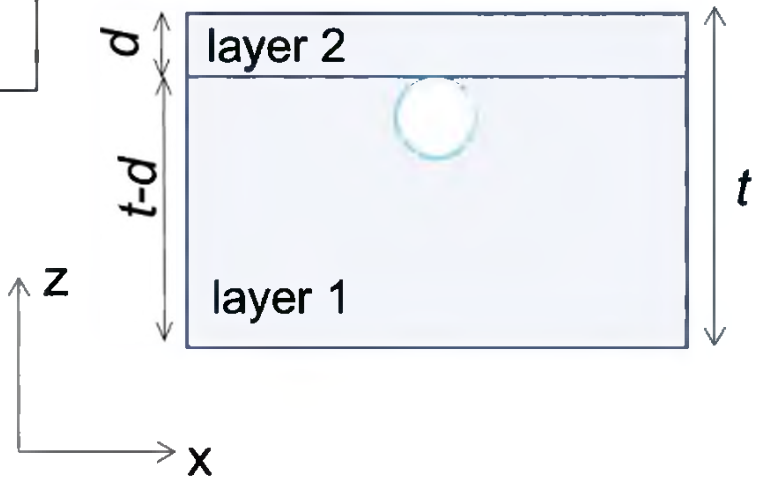

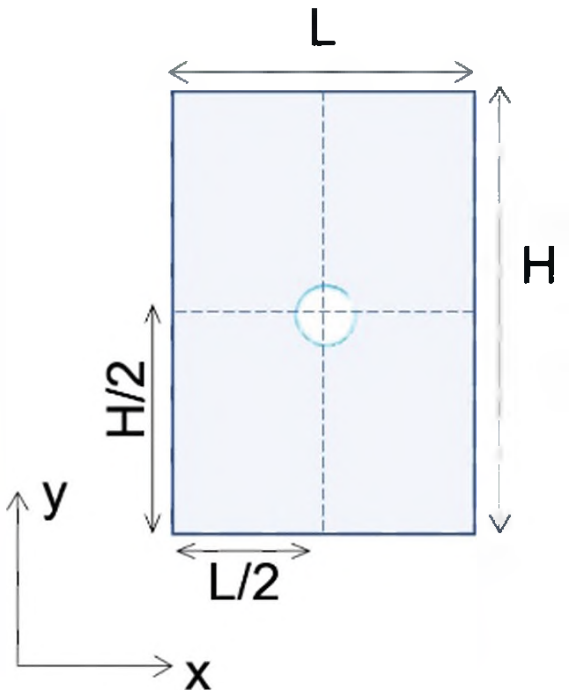

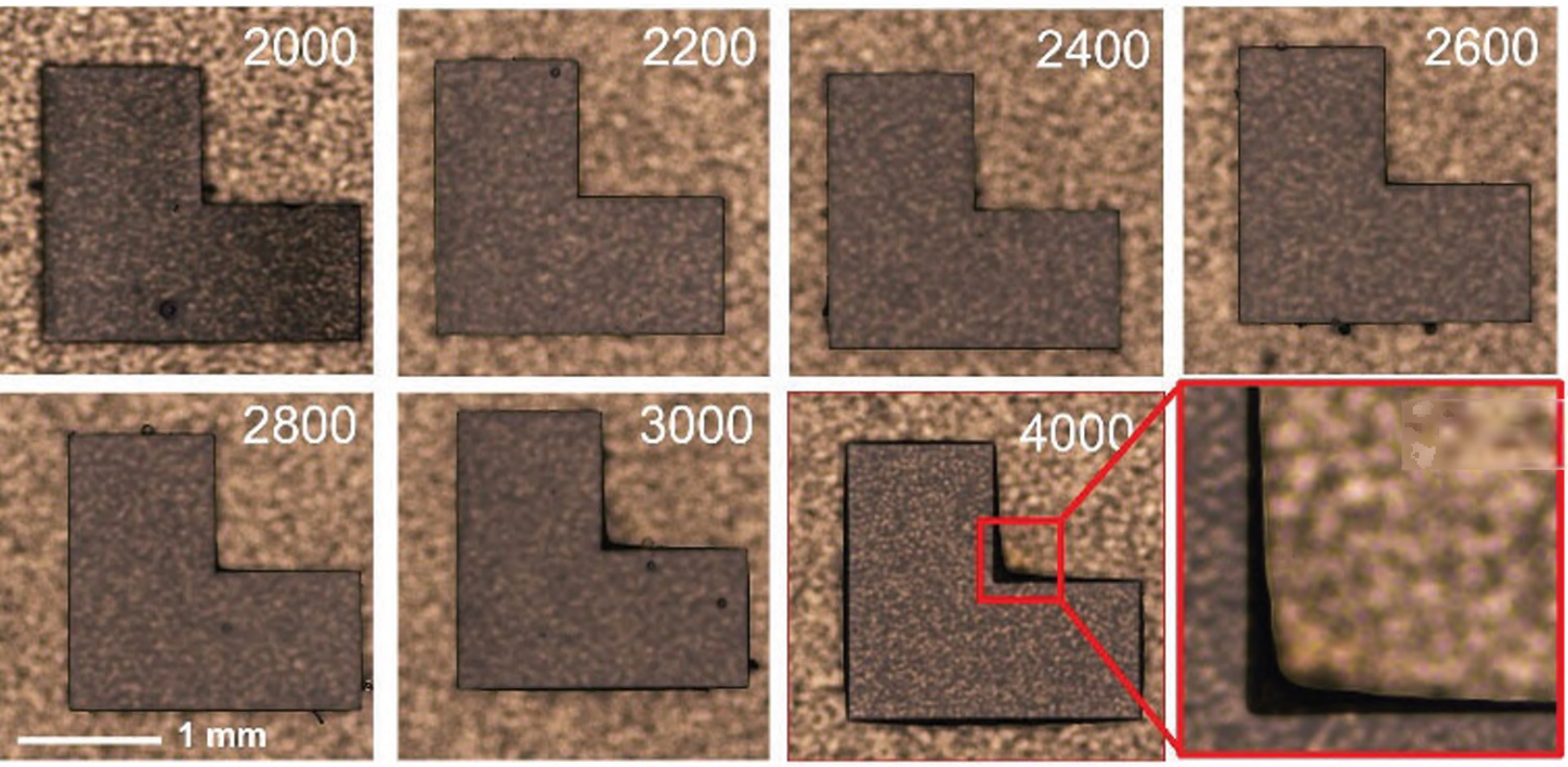
2000
2200
2400
2600
2800
3000
4000
1 mm

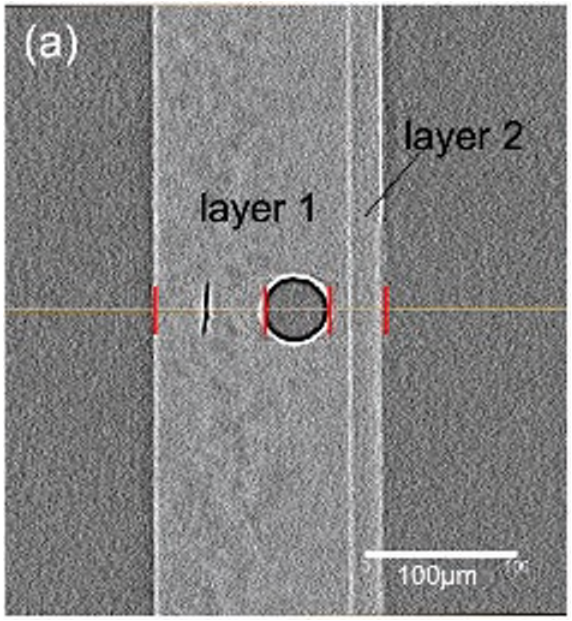
(a)
layer 2
layer 1
100µm

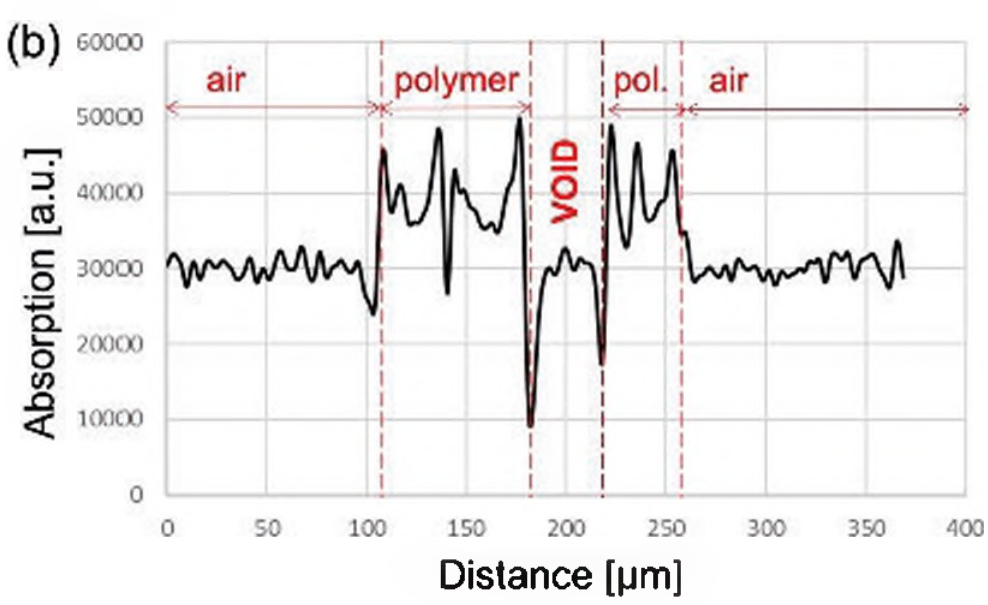
(b)
air
polymer
VOID
pol.
air
Absorption [a.u.]
60000
50000
40000
30000
20000
10000
0
0
50
100
150
200
250
300
350
400
Distance [µm]

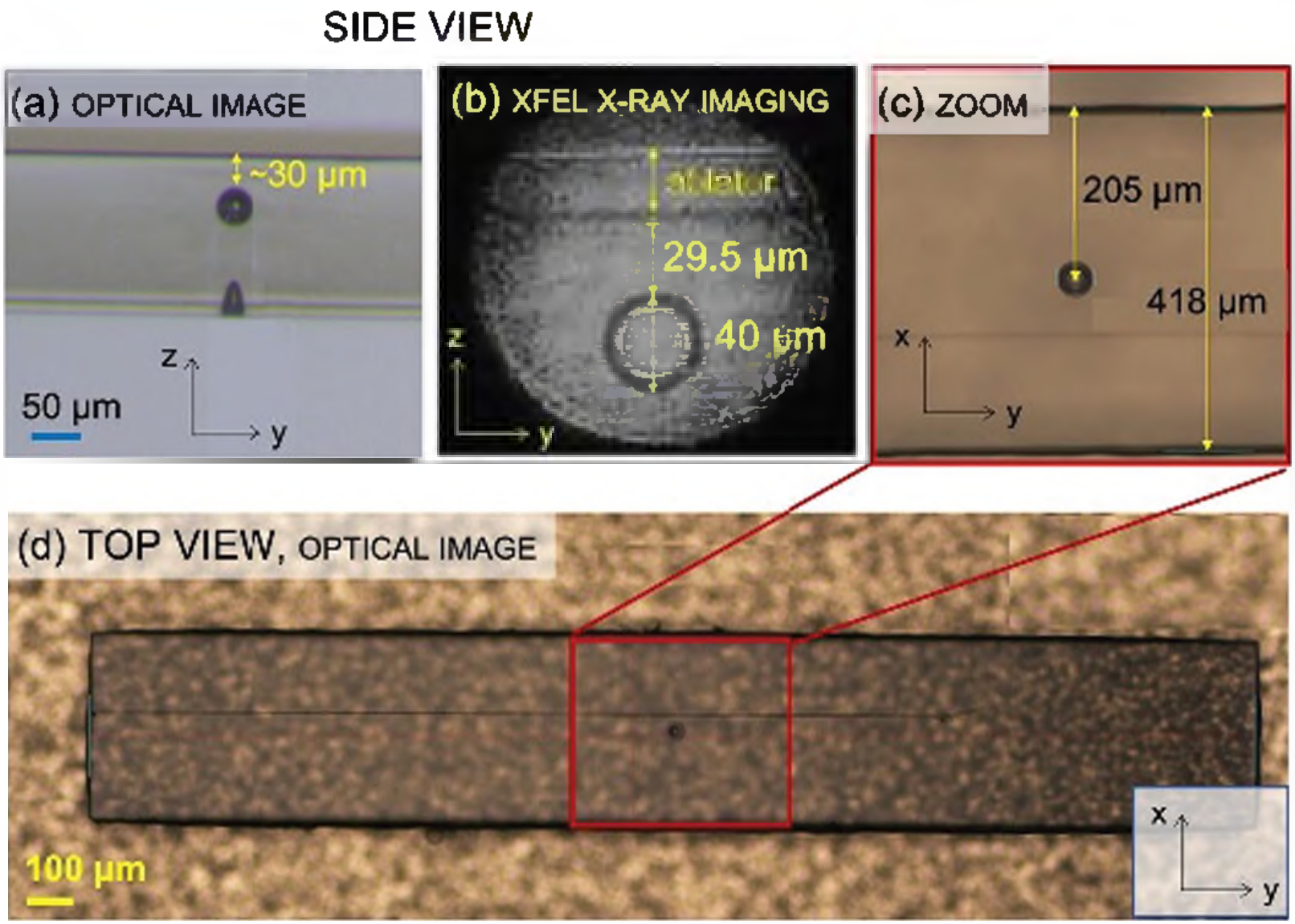
SIDE VIEW
(a) OPTICAL IMAGE
~30 µm
z
y
50 µm
(b) XFEL X-RAY IMAGING
29.5 µm
40 µm
z
y
(c) ZOOM
205 µm
418 µm
x
y
(d) TOP VIEW, OPTICAL IMAGE
100 µm
x
y

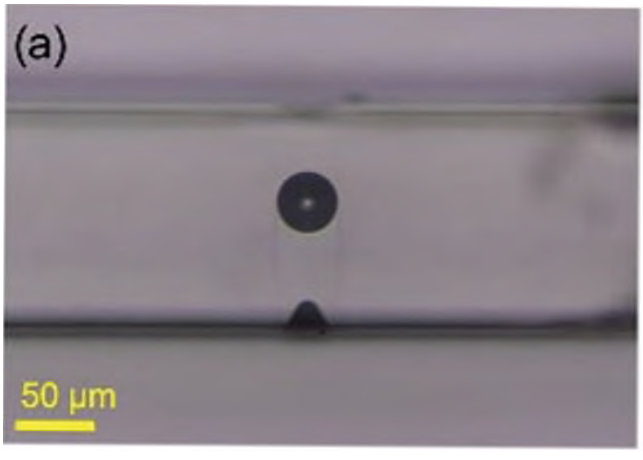
(a)
50 µm


(b)
50 µm